

Numerical investigation of the combustion characteristics and wall impingement with dependence on split-injection strategies from a gasoline direct-injection spark ignition engine

Proc IMechE Part D:
J Automobile Engineering
0(0) 1–18
© IMechE 2013
Reprints and permissions:
sagepub.co.uk/journalsPermissions.nav
DOI: 10.1177/0954407013491216
pid.sagepub.com


Juhyeong Seo, Jae Seong Lee, Kwan Hee Choi, Ho Young Kim and Sam S. Yoon

Abstract

Highly pressurized direct injection applied to automotive vehicles was developed for better power and fuel efficiency, but it causes fuel impingement, which generates more soot emissions. In the present study, analyses of the combustion characteristics and fuel impingement were conducted with a direct-injection spark ignition engine using split-injection strategies. Full three-dimensional unsteady Eulerian–Lagrangian two-phase numerical simulations were carried out to predict the flow field and the combustion characteristics as functions of the injection duration ratio and the weight of the second pulse injection. Experimental data were coupled for verification, providing the boundary and initial conditions for the benchmark case. The results showed that the weight of injection became maximally 35% less as the weight of the second pulse injection decreased. The amount of liquid fuel film, which was influenced by the injection duration ratio, had a varying range from approximately 1% to 4%. When a greater amount of the liquid fuel film impinged on the piston surface, this induced more soot formation. However, the fuel–air mixture was the most prominent factor for determining the overall combustion characteristics. A split injection can increase the thermal efficiency and the fuel consumption rate; however, without optimization, poor combustion characteristics such as knocking, incomplete combustion and soot emissions can result.

Keywords

Spray impingement, liquid fuel film, split injection, gasoline direct injection, direct-injection spark ignition

Date received: 11 October 2012; accepted: 25 April 2013

Introduction

Direct-injection spark ignition (DISI) engines utilize injection technology that optimizes the atomization process during fuel injection. Increasing the injection pressure can produce better atomization^{1,2} and, consequently, a higher compression ratio,^{3,4} a higher thermal efficiency and a better fuel economy.^{5,6} Gasoline DISI engines have a significant potential for increasing the high specific power output by cooling the resident air charge inside the cylinder, which leads to a higher knock-limited compression ratio.⁷ Unfortunately, a high injection pressure induces a higher spray momentum in the fuel, which penetrates through the combustion chamber and impinges on the piston surface or

cylinder walls. This is known as a liquid fuel film (LFF).

When wall wetting happens, the LFF causes a poor evaporation rate, which affects the fuel consumption rate detrimentally.⁸ The impinged fuel that has not evaporated inside the chamber results in several types of emission during the combustion process, such as

School of Mechanical Engineering, Korea University, Seoul, Republic of Korea

Corresponding author:

Ho Young Kim, School of Mechanical Engineering, Korea University, 5-Ga, Anam-dong, Sungbuk-gu, Seoul 136-701, Republic of Korea.
Email: kimhy@korea.ac.kr

unburned hydrocarbons and particulate matter.^{9–11} Wall-wetting observation is difficult to carry out by experimental methods because the phenomenon occurs inside the combustion chamber. A real engine needs a unique structure including an optical window with the ability to tolerate a high pressure and a high temperature in order to observe the phenomenon. The LFF problem is challenging, because the relation between the LFF and emission has not been completely established. Therefore, when fuel is directly injected into the chamber, investigations for minimizing the amount of fuel impingement are needed to advance DISI engine technology.

Several studies have investigated the LFF in gasoline DISI engines through both experimental and numerical methods.^{9–21} Stevens and Steeper¹¹ investigated the imaging of the LFF and the pool fire on top of a piston in a DISI engine experimentally with an optical window using the gasoline laser-induced fluorescence technique. The results indicated that the fuel impingement on the piston was correlated with the injection timing. The existence of the LFF during combustion determined by the injection timing created a pool fire and soot. Han et al.¹² numerically simulated wall wetting and examined the distribution of the fuel–air mixture within the cylinder in a wall-guided stratified DISI engine. The operating conditions were 650 r/min (brake mean effective pressure (BMEP), 1.0 bar; idle), 2500 r/min (BMEP, 1.0 bar; low load) and 2500 r/min (BMEP, 4.0 bar; medium load). The results were induced by parameter changes such as the crank angle (CA) and the swirl control valve position, which improved the fuel impingement and the fuel–air distribution. Drake et al.¹³ applied a refractive-index-matching technique to measure the LFF thickness, the film area and the total LFF volume with different types of high-pressure injector. By switching the injector from a swirl injector to a multi-hole injector, the LFF volumes were dramatically reduced from about 1% (with gasoline fuel) to about 0.1% (with iso-octane). However, the results revealed that the LFF was not the dominant source of hydrocarbon (HC) emissions in the current study (contributing at most 15% for a swirl injector and 2% for a multi-hole injector). The DISI engine was operated at warm-up, steady-state and stratified low-load operating conditions. Park and Ghandhi¹⁴ measured the LFF temperature and thickness on the piston crown using a fibre-based laser-induced fluorescence technique of a wall-guided stratified DISI engine. The operating conditions were under both motored and firing conditions at 600 r/min and 1200 r/min for late injection, using a mixture of iso-octane and a 4% solution of 2,3-hexanedione by volume. The results revealed that the LFF thickness was less than 10 μm for both motoring and fired conditions at the same piston temperature. A number of studies to understand the wall wetting in the intake system have also been made^{15–17} but are not mentioned in this paper.

Considering split injection with high-pressure injection is an advanced solution for improving the characteristics of a DISI engine.^{20–26} A split injection is also effective for reducing the penetration length and causes a reduction in the wall wetting. However, investigations from the viewpoint of wall wetting with a split injection are not as numerous.^{20,21} Serras-Pereira et al.²⁰ carried out visualization of the LFF with a split injection using various engine temperatures and different types of fuel. The engine conditions were 1500 r/min and primarily low-load conditions for both motoring and firing (intake pressure, 0.5 bar). Serras-Pereira et al. found that the LFF was nearly eliminated using a split injection and that the peak heat flux signal due to impingement was related to the relative liquid impact temperature. Yi et al.²¹ numerically demonstrated that the engine output at low-speed and medium-speed wide-open throttle (WOT) conditions can be improved with a split injection. They found that the LFF at 1500 r/min WOT conditions for a single injection reached 0.8%, while that for a split injection (50% of fuel for each pulse) was only 0.1%.

Most previous studies were limited to low-speed low-load operating conditions or to motoring cases, because of the structural problems mentioned. Previous numerical studies investigated high-speed high-load conditions, but low-speed high-load conditions have rarely been studied. Most results regarding the LFF for a split injection have not reported results for soot and other kinds of emission such as nitrogen oxide (NO_x) emissions.

The objective of this study is to investigate the effects of split-injection strategies on reducing the LFF and improving the emissions and thermal efficiency in the low-speed high-load region in order to enhance the gasoline DISI engine performance. The present work focuses on a concrete investigation of the LFF, the fuel–air distribution and the relations with the soot emissions using split-injection strategies for low-speed high-load operating conditions, to contribute to reduction in the emissions and to increase the engine torque. The main parameters for the split injection were varied by the weight of the fuel injection and the injection duration of the second pulse for the same amount of fuel during the injection. The results reveal how the flow field and the split-injection strategies influence the LFF and their relations to the soot emissions. Additional results such as the distribution of the fuel–air mixture before ignition are also examined, as it is equally important. The results of this work can be applicable to real wall-guided gasoline DISI engines. Moreover, low-speed high-load operation conditions in a gasoline DISI engine can be coupled with downsizing, which is key to addressing the fuel economy issues.^{27–29} First, the numerical results are verified by comparison with experimental data for a single injection. When a split injection is employed, the weight of the injection and the injection duration ratio of the second pulse were changed from 30% to 70% and from 0.5 to 1.5

Table 1. Engine specifications.

Parameter	Specification
Number of cylinders	4
Bore	88 mm
Stroke	97 mm
Compression ratio	11.3
Valves	Two intake, two exhaust
Valve timing	Intake, variable valve timing; exhaust, variable valve timing
Fuel injection guidance type	Wall guided
Displacement	2359 cm ³

respectively. Finally, the optimum conditions within the investigated cases are discussed.

Methodology

To investigate the combustion characteristics and wall impingement using the effects of split-injection strategies, a single-cylinder engine was utilized. The single-cylinder engine was based on a four-stroke gasoline DISI engine with the detailed engine specifications given in Table 1.

Governing equations

Fuel injected in a cylinder is considered as a multi-phase flow problem that can be approached as a Eulerian–Lagrangian problem. The governing equations in the continuous phase involve the mass, momentum, energy and species conservation equations and are defined by

$$\frac{\partial}{\partial t}(\rho) + \frac{\partial}{\partial x_j}(\rho u_j) = S_d \quad (1)$$

$$\begin{aligned} \frac{\partial}{\partial t}(\rho u_i) + \frac{\partial}{\partial x_j}(\rho u_j u_i) &= -\frac{\partial P}{\partial x_i} \\ &+ \frac{\partial}{\partial x_j} \left[\mu_e \left(\frac{\partial u_i}{\partial x_j} + \frac{\partial u_j}{\partial x_i} \right) - \frac{2}{3} \left(\rho k + \mu_e \frac{\partial u_k}{\partial x_k} \right) \delta_{ij} \right] + S_i \end{aligned} \quad (2)$$

$$\begin{aligned} \frac{\partial}{\partial t}(\rho h) + \frac{\partial}{\partial x_j}(\rho h u_j) &= \frac{\partial}{\partial x_j} \left[\left(\frac{\lambda}{c_p} + \frac{\mu_t}{\sigma_h} \right) \frac{\partial h}{\partial x_j} \right] \\ &+ \frac{\partial P}{\partial t} + u_j \frac{\partial P}{\partial x_j} \\ &+ \frac{\partial u_i}{\partial x_j} \left[\mu_e \left(\frac{\partial u_i}{\partial x_j} + \frac{\partial u_j}{\partial x_i} \right) - \frac{2}{3} \left(\rho k + \mu_e \frac{\partial u_k}{\partial x_k} \right) \delta_{ij} \right] \\ &- \frac{\partial}{\partial x_j} (h \rho Y V_j) + S_h \end{aligned} \quad (3)$$

$$\begin{aligned} \frac{\partial}{\partial t}(\rho Y) + \frac{\partial}{\partial x_j}(\rho u_j Y) &= \frac{\partial}{\partial x_j} \left(\frac{\mu_t}{\sigma_Y} \frac{\partial Y}{\partial x_j} \right) \\ &- \frac{\partial}{\partial x_j} (\rho Y V_j) + S_m \end{aligned} \quad (4)$$

where μ_e , μ_t , σ_h , σ_Y , δ_{ij} , V_j and k are the effective viscosity, the turbulent viscosity, the turbulent Prandtl

number for the energy equation, the turbulent Prandtl number for the species equation, the Kronecker delta and the j component of the diffusion velocity respectively. The symbols S_d , S_i , S_h and S_m represent the source terms from each governing equation for the continuous phase.

For the equations of the dispersed phase, the momentum equation and the displacement of the droplet are expressed as

$$m_d \frac{du_{di}}{dt} = \frac{1}{2} C_D \rho A_d |u_i - u_{di}| (u_i - u_{di}) - V_d \nabla p \quad (5)$$

and

$$\frac{dx_{di}}{dt} = u_{di} \quad (6)$$

respectively, where x_{di} and u_{di} are the displacement and the droplet velocity respectively. The drag coefficient C_D in the momentum equation was correlated by Yuen and Chen.³⁰ The mass and the heat transfer of a droplet in the boiling condition are calculated from

$$\begin{aligned} \frac{dm_d}{dt} &= -2\pi \frac{\lambda}{c_p} D_d (1 + 0.23 Re^{0.5}) \\ &\ln \left[1 + \frac{c_p (T - T_d)}{h_{fg}} \right] \end{aligned} \quad (7)$$

and

$$m_d c_{p,d} \frac{dT_d}{dt} = -A_S q_d'' + h_{fg} \frac{dm_d}{dt} \quad (8)$$

respectively.

Modelling descriptions

Our research includes specific types of model and sub-model that are able to describe the spray atomization, wall wetting, fuel–air distribution, combustion process including knocking, etc. First, for droplet break-up and atomization, a Reitz–Diwakar³¹ model has been adopted. The relation between a droplet and the cylinder wall for impingement was estimated by the Bai–Gosman^{32,33} model, which can reveal the liquid film mass, the liquid film thickness and the droplet post-impingement characteristics. Collision and fusion between each droplet from fuel injection follows the O'Rourke³⁴ model for the general interaction. Our study is based on a three-dimensional (3D) Reynolds-averaged Navier–Stokes formulation employing the k – ϵ renormalization group turbulence model.³⁵

For the combustion model, the three-zone extended coherent flame model was adopted.^{36,37} The laminar flame speed model proposed by Metghalchi and Keck³⁸ was used. The post-flame chemistry including emission formation was studied using the soot model developed by Patterson et al.³⁹, and the nitric oxide formation model was proposed using the three extended Zeldovich mechanisms.

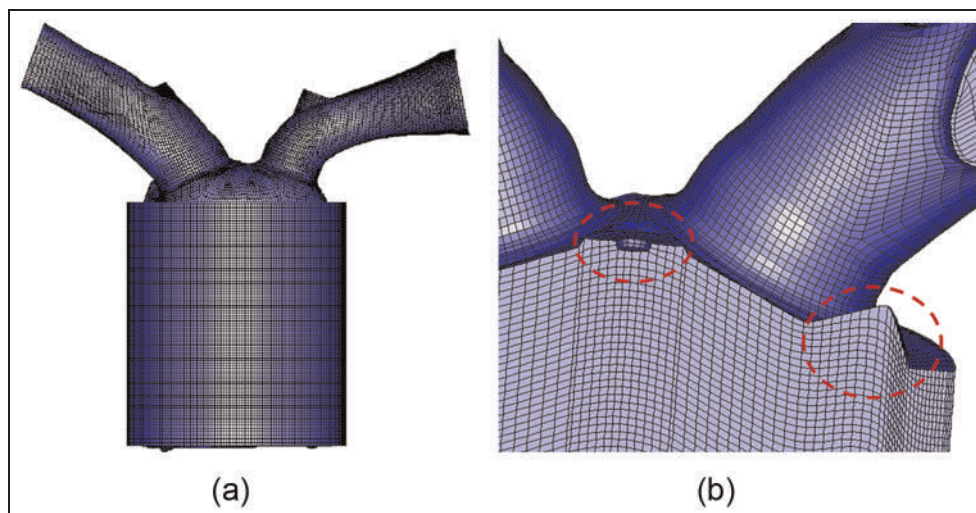


Figure 1. (a) Grid generation of the cylinder, the intake port (left) and exhaust port (right), the injector, the piston surface, the combustion dome and the spark plug. (b) Zoomed view of the spark plug and the injector.

Geometry and mesh generation

The present numerical work simulated a full 3D generated modelling from the computer-aided design geometry by applying a moving mesh. Figure 1 shows the generated geometry for the current computational domain. Symmetry conditions were applied to the computational domain for simplification; therefore, just half of the combustion chamber was considered with an intake port and an exhaust port. The port on the left-hand side in Figure 1(a) is the intake port, and that on the right-hand side is the exhaust port. The moving mesh reflects the change in the computational domain with time due to the moving parts such as the piston, the valves and the cylinder wall. The current injector is a side injection type mounted between the intake ports, and injection fuel was targeted towards the piston bowl. The operational fuel pressure of the solenoid injector was increased up to 150 bar with six holes in the symmetrical pattern. The spray cone angle ranged from 35° to 80° , which yielded the solid cone pattern. The Sauter mean diameter (SMD) was less than $22\ \mu\text{m}$ under a fuel injection pressure of 150 bar. The SMD for the current study ranged from $9\ \mu\text{m}$ to $30\ \mu\text{m}$ (the average SMD in all cases is $19.7\ \mu\text{m}$) during our numerical studies. A single spark plug was placed at the top of the combustion chamber but slightly closer to the intake port than to the exhaust port, as shown in Figure 1(b). For all computations, the number of cells for this study depended on the position of the piston by applying moving mesh generation. When the piston is at the top dead centre (TDC) position, the grid resolution is approximately 164,500 nodes and increases to about 344,000 nodes at the bottom dead centre (BDC) position.

Boundary and operating conditions

Most data used for the initial and boundary condition were obtained from the experimental data for actual

operating conditions when the engine was fully warmed. The intake and exhaust pressures and temperatures were measured with a manifold air pressure sensor and K-type thermocouple. Their corresponding values were 0.95 bar, 1.01 bar, 300 K and 898 K respectively. Each pressure and temperature were measured for 60 s and the averaged values were used. However, the temperatures of each of the valves and the cylinder wall were estimated owing to difficulties in making measurements at their locations. The boundary conditions for the temperatures of the combustion dome, the cylinder wall, the piston crown and the valve were estimated to be 400 K, 450 K, 460 K and 800 K respectively.^{40,41} An injection temperature of 330 K was used, except for the simulation verification case described in a later section. The engine operating speed condition was 2000 r/min with the WOT operation condition. Gasoline with an octane number of 92 was used as the working fuel for the experimental results in the real engine. Isooctane was used in the simulation to represent gasoline, and the octane number was changed to 92 to predict the knock phenomenon more accurately. The spray characteristics of isooctane have shown consistent similarities to those of gasoline, and isooctane can therefore be used as a surrogate for gasoline at WOT operating conditions.^{42,43}

Numerical procedures

The simulations were performed using a commercial code. For the convective differencing process, the monotone advection and reconstruction scheme was applied.⁴⁴ The pressure implicit with splitting of operators (PISO) algorithm was also utilized. PISO was applied on the basis of a fully implicit scheme for a time-marching calculation. The operating time step for the investigation is $\Delta t = 0.1^\circ\ \text{CA}$, corresponding to $t = 8.33\ \mu\text{s}$. Figure 2 compares the grid sensitivity

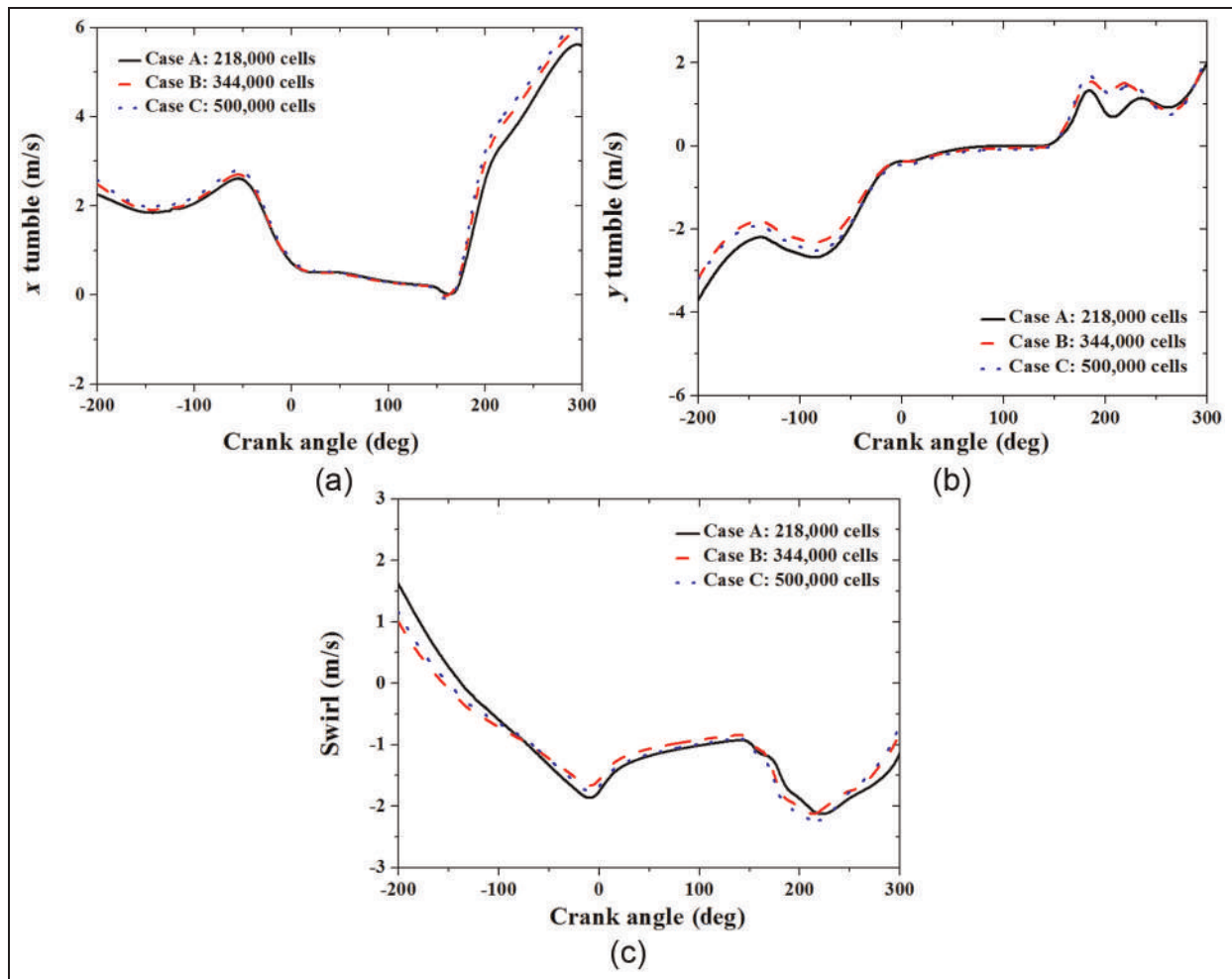


Figure 2. Computational results with various numbers of cells for the grid systems: (a) x tumble; (b) y tumble; (c) swirl.

Table 2. Model results compared with the experimental data.

	Experimental data	Present results	Error (%)
Peak heat release rate (J/deg CA)	33.85	34.53	2.01
Peak in-cylinder pressure (bar)	43.19	40.06	7.25
Intake air mass (mg/stroke)	296.22	291.92	1.45
Polytropic index (compression stroke)	1.30	1.34	3.08
Polytropic index (expansion stroke)	1.33	1.28	3.76

studies of flow field characters (swirls) for different cases. A very weak difference can be seen between case B and case C. A resolution of 344,000 at BDC yielded an acceptably accurate solution for the calculation domain. Estimating the relation between the generated mesh and the time step dependence, the mean Courant number was monitored throughout the study. The mean Courant number from the computational domain during the study was always smaller than 1 in all cases, which decreases oscillations and improves the accuracy of the results. The computational run time is approximately 75 h per case, totalling approximately 2100 h using two Intel Zeon E5630 2.53 GHz processors (eight cores) and a random-access memory of 16 Gbytes.

Results and discussion

Verification

For verification, the results were obtained and compared with the experimental data in the same operation conditions. The numerical results of the in-cylinder pressure, the heat release rate (HRR), the $\log(\text{pressure})-\log(V/V_{max})$ diagram and the intake air mass were resolved and compared with the experimental data. The operation conditions were the start of injection (SOI) at 300° CA before top dead centre (BTDC), $\lambda = 0.838$ and an Spark Advance (SA) of 12.44° CA BTDC; the other conditions were as mentioned above. The experimental values of the in-cylinder pressure and the HRR

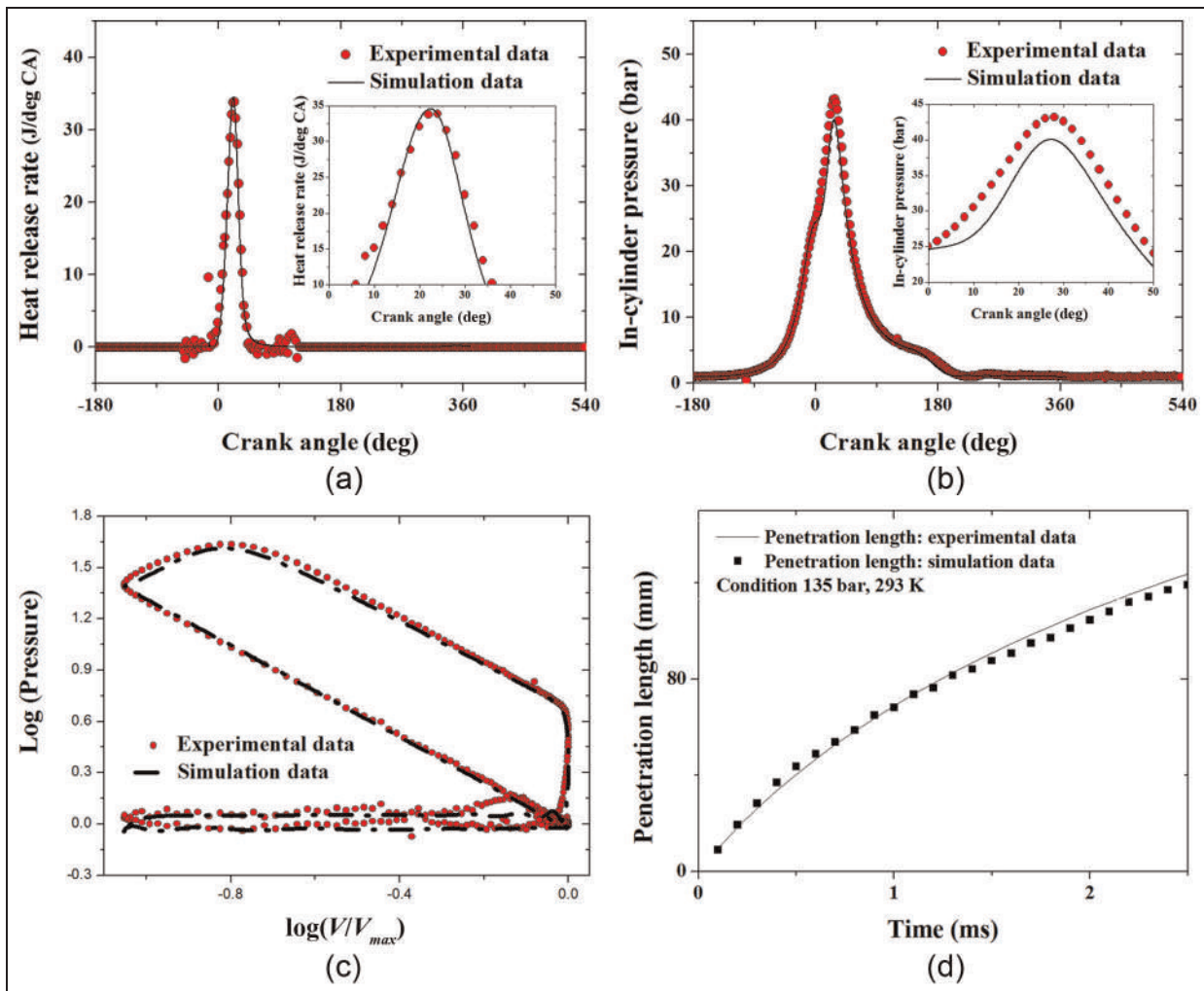


Figure 3. Comparison between the experimental data and the simulation results: (a) the HRR (red full circles, experimental data; solid curve, simulation data); (b) the in-cylinder pressure (red full circles, experimental data; solid curve, simulation data); (c) the $\log(\text{pressure})-\log(V/V_{max})$ (red full circles, experimental data; dash-dotted curve, simulation data); (d) the penetration length at atmospheric conditions ($P_{inj} = 135 \text{ bar}$; $T_{inj} = 293 \text{ K}$) (solid curve, experimental data; full squares, simulation data). CA: crank angle.

were the average values over 50 cycles for each CA. The intake air masses obtained from the experimental values were the average amounts during the intake stroke of 50 cycles. Figure 3(a), (b) and (c) shows the results of the HRR, the in-cylinder pressure and the $\log(\text{pressure})-\log(V/V_{max})$ diagram respectively. The overall tendencies of the values were similar to those of the experimental data. The maximum values had slight deviations of 2.00% and 7.25% for each HRR and in-cylinder pressure respectively. In addition, the differences between the intake air mass and the polytropic index are listed in Table 2.

The second verification case of the penetration length of fuel injection from the experimental results was compared with the present numerical estimates. The atmospheric pressure and the atmospheric temperature were maintained at 1 bar and 293 K respectively for both the experiments and the numerical simulations. The fuel injection was conducted at 135 bar and 293 K. As shown in Figure 3(d), the

penetration length during injection matched the experimental data well.

Spray and impingement development

Figure 4 shows the process of spray formation and fuel impingement during fuel injection for the verification case. The injection fuel was targeted towards the piston bowl. While injecting fuel, the region of wetted impingement area expanded on the piston crown. It is noteworthy that the view of six fuel injector holes is obscured by the droplets which are purposely over-scaled for clear presentation of the atomization process. The simulation incorporated the geometry of the actual six injectors used in the relevant experiments.

Parametric studies

In order to find an appropriate case to enhance the performance of the engine with the model established in

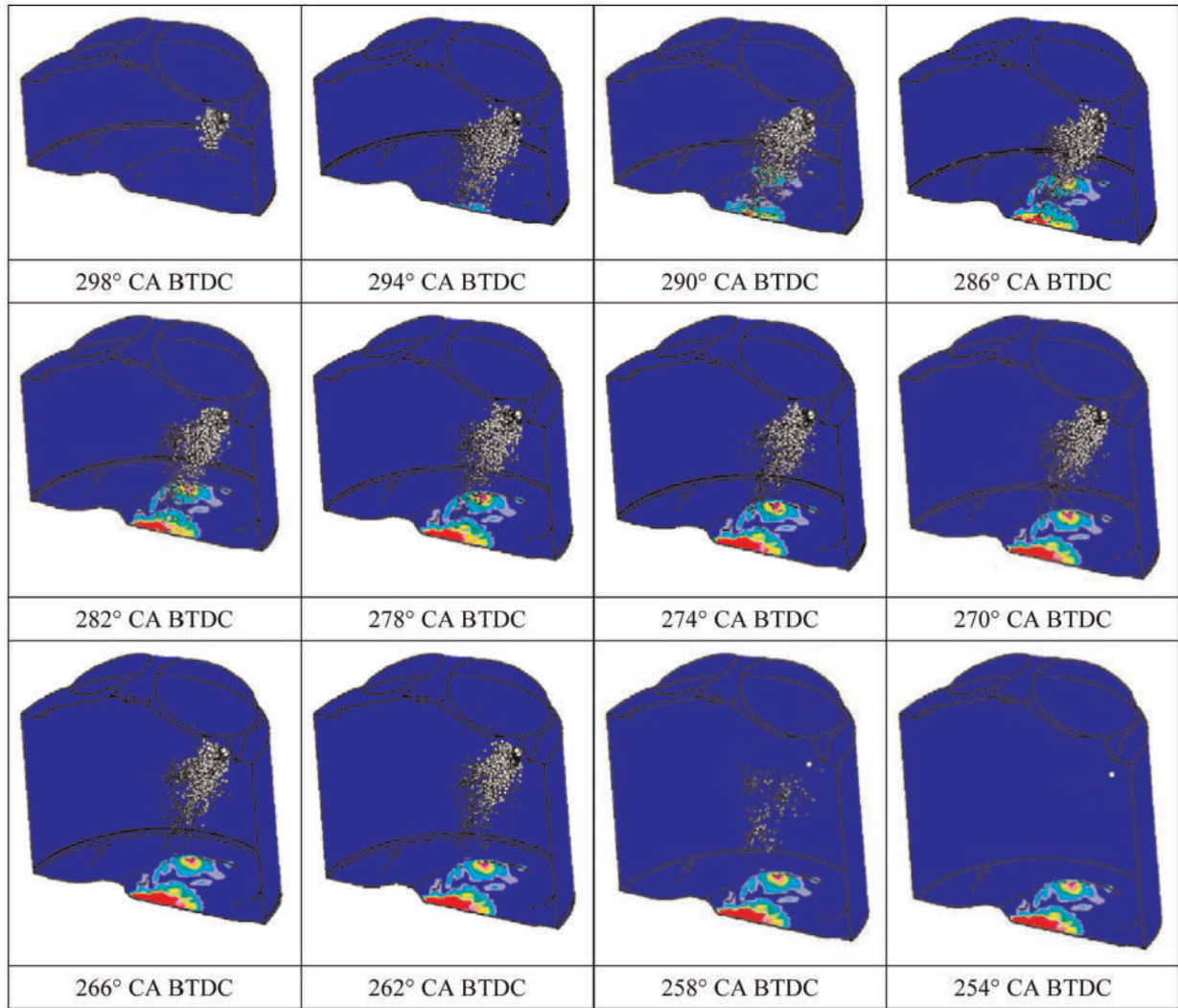


Figure 4. Process of the simulated spray formation and impingement at various CAs.
CA: crank angle; BTDC: before top dead centre.

this study, a set of parametric studies was executed on the effects of the weight of the injection and the injection duration ratio of the second pulse injection. The weight of the injection and the injection duration ratio were varied from 30% to 70% and from 0.5 to 1.5 respectively, as in Table 3. The notation for each case was written in the form D-40-0.5, which means that 40% of the total mass was injected during the second pulse injection using only the half-duration.

Effect of split injection

In wall-guided engines, the vortical motion in the Z - X plane, called 'y tumble', can represent the characteristics of the velocity flow field. The vertical motion in the Z - X plane can be defined as⁴⁵

$$y \text{ tumble} = \frac{\sum_{N_{cells}} m_i [(Z_i - Z_m)u_i - (X_i - X_m)w_i]}{\sum_{N_{cells}} m_i \sqrt{(X_i - X_m)^2 + (Z_i - Z_m)^2}} \quad (9)$$

where N_{cells} is the number of cells within the combustion chamber, m_i is the mass within each cell, (x_i, y_i, z_i) are the Cartesian coordinates of the local cell centroid and (u_i, v_i, w_i) are the velocity components of the local cell. The positive value and the negative value of y tumble imply a clockwise flow field and a counterclockwise flow field respectively. Figure 5(a), (b) and (c) represents the plots of the y -axis tumble number as a function of the CA during the intake and compression stroke by varying the injection duration ratio at 30% of the weight of the second injection, 50% of the weight of the second injection and 70% of the weight of the second injection respectively. While decreasing the weight of the second injection, the y -tumble value temporarily increases from 0.396 to 1.045 and then to 1.546. The counterclockwise flow field inside the combustion chamber weakens (or changes to the clockwise flow field) during the clockwise flow injection. On the other hand, the air entering during the intake stroke makes the flow field negative, and the y tumble has a counterclockwise

Table 3. Operation condition for split-injection strategy.

Weight of the second injection (%)	First injection		Second injection		Notation
	SOI (deg CA BTDC)	Duration (deg CA)	SOI (deg CA BTDC)	Duration (deg CA)	
30	310	26.18	130	5.61	D-30-0.5
30	310	26.18	130	8.41	D-30-0.75
30	310	26.18	130	11.22	D-30-1.0
30	310	26.18	130	14.02	D-30-1.25
30	310	26.18	130	16.83	D-30-1.5
40	310	22.44	130	7.48	D-40-0.5
40	310	22.44	130	11.22	D-40-0.75
40	310	22.44	130	14.96	D-40-1.0
40	310	22.44	130	23.37	D-40-1.25
40	310	22.44	130	22.44	D-40-1.5
50	310	18.70	130	9.35	D-50-0.5
50	310	18.70	130	14.02	D-50-0.75
50	310	18.70	130	18.70	D-50-1.0
50	310	18.70	130	23.37	D-50-1.25
50	310	18.70	130	28.05	D-50-1.5
60	310	14.96	130	11.22	D-60-0.5
60	310	14.96	130	16.83	D-60-0.75
60	310	14.96	130	22.44	D-60-1.0
60	310	14.96	130	28.05	D-60-1.25
60	310	14.96	130	33.66	D-60-1.5
70	310	11.22	130	13.09	D-70-0.5
70	310	11.22	130	19.63	D-70-0.75
70	310	11.22	130	26.18	D-70-1.0
70	310	11.22	130	32.72	D-70-1.25
70	310	11.22	130	39.26	D-70-1.5

SOI: start of injection; CA: crank angle; BTDC: before top dead centre.

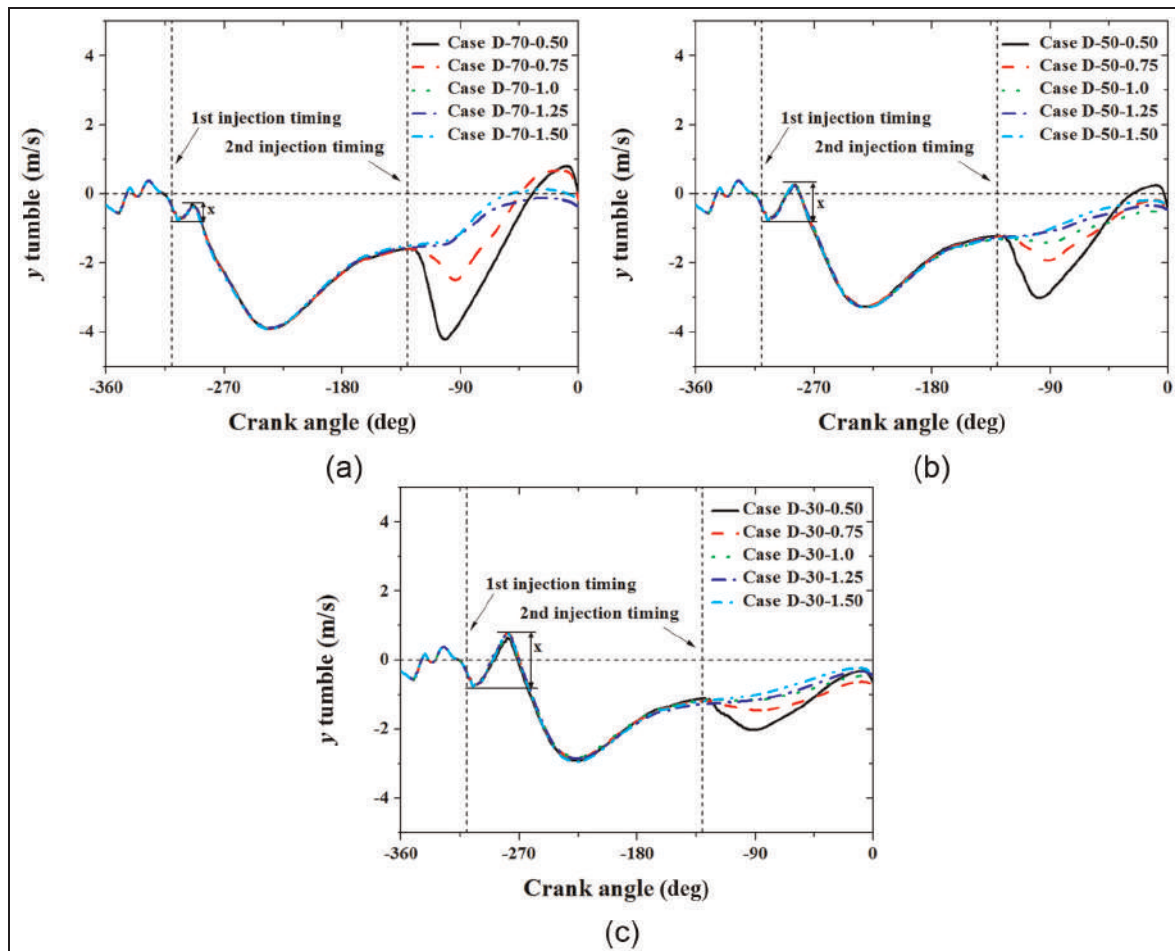


Figure 5. Variation in the y -tumble number with the CA: (a) 70% of the weight of the second injection; (b) 50% of the weight of the second injection; (c) 30% of the weight of the second injection.

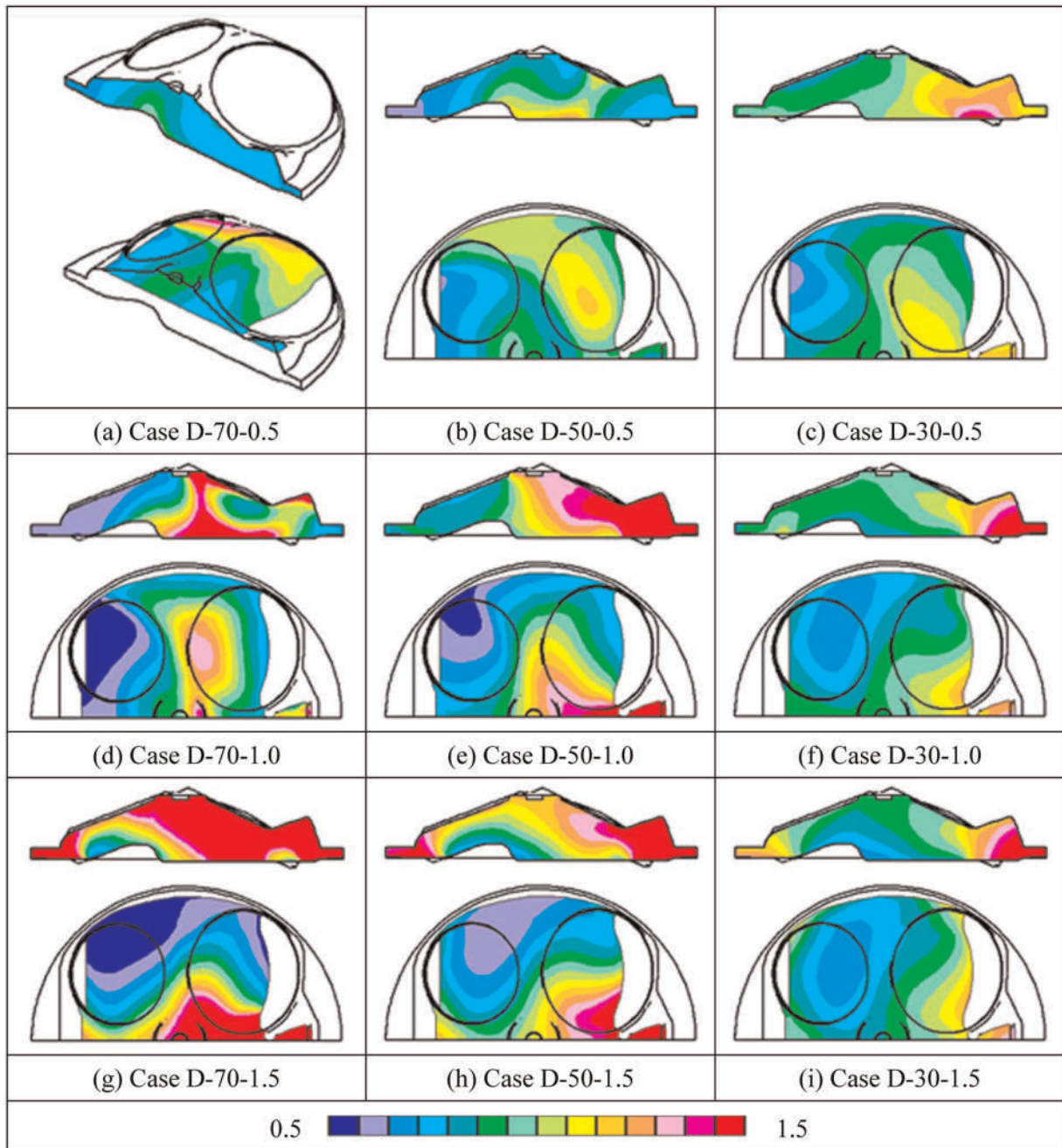


Figure 6. Images of the excess air ratio λ distribution inside the combustion chamber for various cases (14° CA BTDC).

flow field structure. As the second pulse injection proceeds, the counterclockwise flow varied much more when the injection duration ratio was small. Because more fuel was injected at 70% of the weight of the second injection, the counterclockwise flow field varied by even more than 50% and 30%. At TDC (or 0° CA BTDC), the y tumble was close to zero but, as the weight of the second injection increased, the y -swirl flow field occurred more frequently.

The distribution of the excess air ratio λ inside the combustion chamber is described in the Z - X plane and the X - Y plane, as shown in Figure 6. The excess air ratio distribution formation was at 14° CA BTDC,

which is just before ignition; the SA was 12.44° CA BTDC. As the weight of the second pulse injection or the injection duration ratio increases, the tendency of the excess air ratio assumes a higher value near the spark plug. Therefore, case D-70-1.5 had the highest excess air ratio near the spark plug owing to combination of the two parameters. The cases that had a high excess air ratio near the spark plug also had a low value of the excess air ratio near the exhaust liner, showing poor mixing distribution.

In an effort to understand the mixing processes better, the uniformity index r is used to represent the mixing quality.⁴⁶ Figure 7 shows a plot of the uniformity

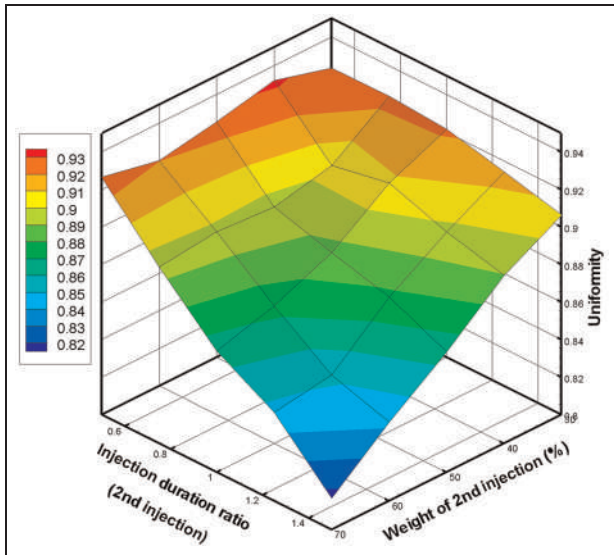


Figure 7. Uniformity index as a function of the injection duration ratio and the weight of the second injection on the contour plot (15° CA BTDC).

index r for the cases just before ignition at 15° CA BTDC. The uniformity index is calculated as

$$r = 1 - \frac{1}{2n} \sum_{i=1}^n \frac{\sqrt{(C_i - C)^2}}{C_i} \quad (10)$$

where C_i and C are the local fuel mass fraction and the average fuel mass fraction respectively. When the uniformity index is close to 1, the fuel distribution is homogeneous and, when the uniformity index is close to 0, the fuel concentrates in a local area. The tendency of the uniformity shows the lowest value, 0.817, in case D-70-1.5, which is approximately 12.3% less than the highest case (D-40-0.5; uniformity index, 0.932). Figure 7 is evidence of the explanation of Figure 6 and shows a tendency coincident with that of the uniformity index. The reason is that the mixing process has insufficient time owing to the short mixing duration of the fuel injection when the weight of the second injection or the injection duration ratio increases. Moreover, the slope from each weight of the second injection or the injection duration ratio becomes steeper as each parameter increases. The average slope for each weight of the second pulse injection is varied from -0.0008 to -0.02243 for the weight of the second injection, and the injection ratio is varied from -0.0043 to -0.00275 .

The LFF formation contour and the total amount located on the piston surface are illustrated in Figure 8 and Figure 9 respectively. Both Figure 8 and Figure 9 show the process at 15° CA BTDC before ignition. In Figure 8, the shapes of LFF formation on the piston surface were similar for all cases, but there was more LFF deposit on the piston surface, as the weight of the second

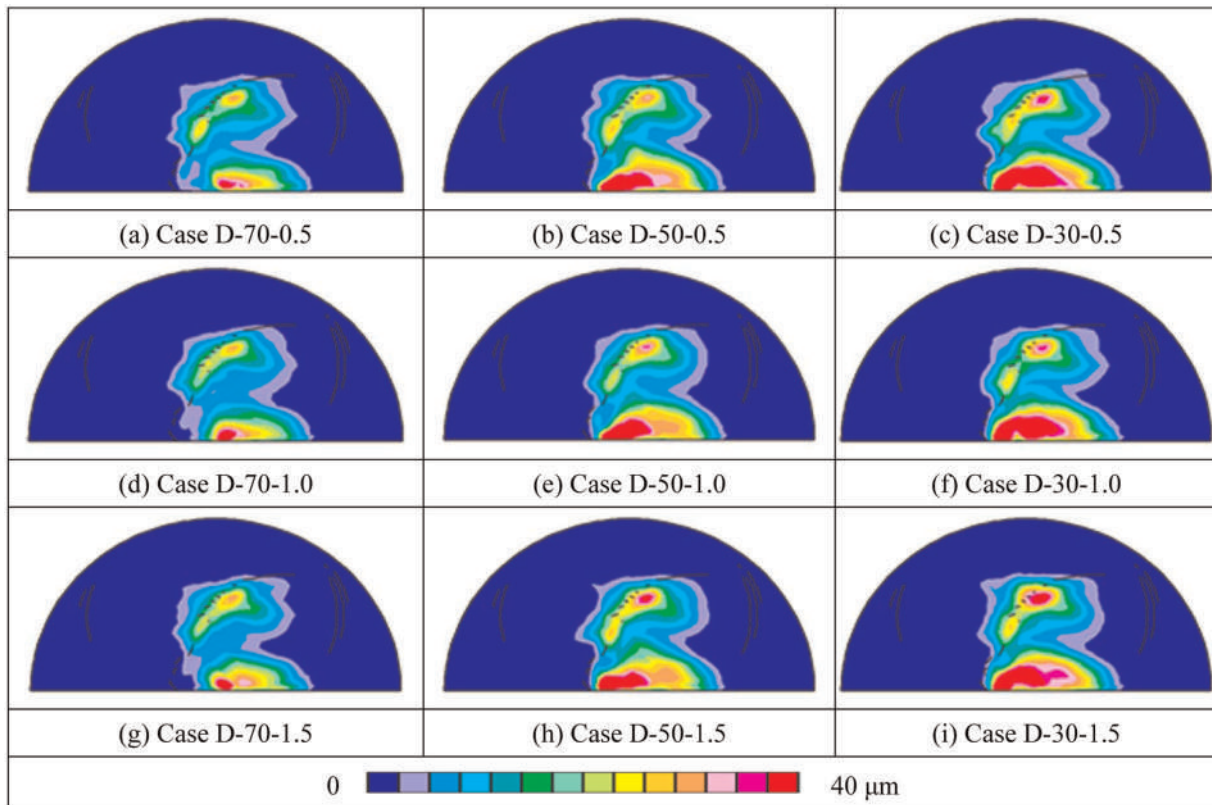


Figure 8. Images of the fuel film thickness distribution on the piston surface, showing the effects of the injection duration ratio and the weight of the second injection for various cases.

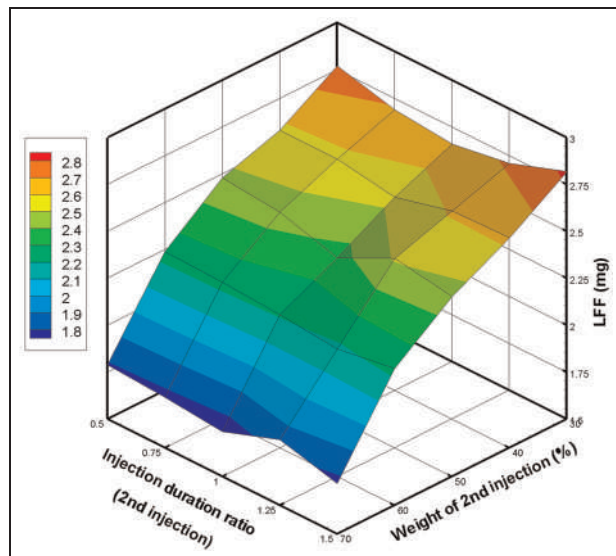


Figure 9. Contour plot of the LFF mass on the piston surface (15° CA BTDC).
LFF: liquid fuel film.

injection decreased. The first pulse injection was injected at 310° CA BTDC, where the piston surface is close to TDC, and the direction of the injector was towards the piston bowl; therefore more LFF formed when the weight of the first pulse injection increased. The effect of the injection duration ratio is easier to observe in Figure 9. When the injection duration ratio is low, the fuel of the second pulse injection was injected in a relatively short amount of time with a high momentum and impinged on the piston surface. In contrast, fuel was injected over a relatively long period; therefore, even though the second pulse injection had a lower momentum, there was more time for the LFF to impinge on the piston surface when it was closer to the TDC. Therefore, the appropriate injection duration was an injection duration ratio of 1.0. The LFF amount for 70% of the weight of the second injection was approximately 31.7–37.5% less than for 30% of the weight of the second injection. The range of the amounts of LFF varies maximally by 4% owing to the influence of the injection duration ratio.

The phenomenon of knocking was demonstrated in some cases by observations of the HRR. Figure 10(a) and (b) shows the HRR during the compression and combustion stroke by varying the weight of the second injection at injection duration ratios of 0.5 and 0.75 respectively. In the cases where knocking occurred, the HRR was first observed to rise as the combustion started and then sharply to increase once more by knocking. When the weight of the second injection was increased, a sharp increase in the HRR by knocking occurred even more, but there was almost no negative effect of knocking on the HRR history, as shown for cases D-30-0.5, D-30-0.75, D-40-0.75 and D-50-0.75. The knocking phenomenon occurred when the peak HRR caused by combustion was larger than 42.5 J/deg

CA. No knocking phenomenon was detected for the other cases not shown in Figure 10(a) and (b). Figure 10(c) shows the oxygen mass fraction obtained at an injection duration ratio of 0.5, which represents the combustion speed during the combustion process. The oxygen mass fraction decrement period was shorter because the combustion speed was faster as the weight of the second injection increased. The turbulence intensity is shown in Figure 10(d), indicating faster combustion. The turbulence intensity became higher as the weight of the second injection increased. Figure 10(d) also shows the averaged in-cylinder temperature in order to estimate the cooling effect due to direct injection. The cooling effect was prominent when the averaged in-cylinder temperature was reduced. The average in-cylinder temperature was measured just before the ignition and the values of each case at an injection duration ratio of 0.5 were 736.49 K, 738.09 K, 737.72 K, 736.48 K and 736.79 K. The variation between each value in the 0.5 injection duration ratio cases stayed minimal at 0.22%; thus the cooling was dominated by the second injection. Therefore, the knocking phenomenon was most influenced by the combustion speed, rather than by the cooling effect.

Figure 11(a) and (b) represents the peak HRR plot and the in-cylinder pressure plot respectively. The dash-dotted curve in Figure 11(a) divides the HRR plot into two parts; a regime in which knocking had an effect (high-value regime), and a regime with little or no knocking effect (low-value regime). Both the HRR and the in-cylinder pressure had similar tendencies for the ranges of parameters investigated; the in-cylinder pressure also has a high value in the knocking regime. The tendencies of both the HRR and the in-cylinder pressure were significantly related to the distribution of the excess air ratio λ shown in Figure 6. Case D-70-1.5 had an excessive amount of air just beside the spark plug, which induced poor combustion. Therefore, the HRR and the in-cylinder pressure without appropriate control can bring about poor combustion characteristics; the peak HRR and the in-cylinder pressure for a single injection were 37.04 J/deg CA and 43.94 bar at an SOI of 310° CA BTDC with the same fuel amount and conditions as in the split-injection case.

Figure 12 shows the configuration of the soot mass fraction, demonstrating the progress of soot generation within the combustion chamber during the combustion and exhaust stroke. Two primary soot sources were identified owing to incomplete combustion (or a locally rich gaseous mixture), as well as pool fires fed by the LFF on the piston.¹⁰ The main process of soot generation can be represented by two scenarios in our investigation. Case D-70-1.5 represents the first scenario, in which soot is generated inside the combustion chamber and near the piston bowl, caused by both a locally rich gaseous mixture and a pool fire. The other scenario, case D-30-0.5, has soot generation only around the piston bowl. The history of the soot mass in the combustion chamber is shown in Figure 13; the cases not

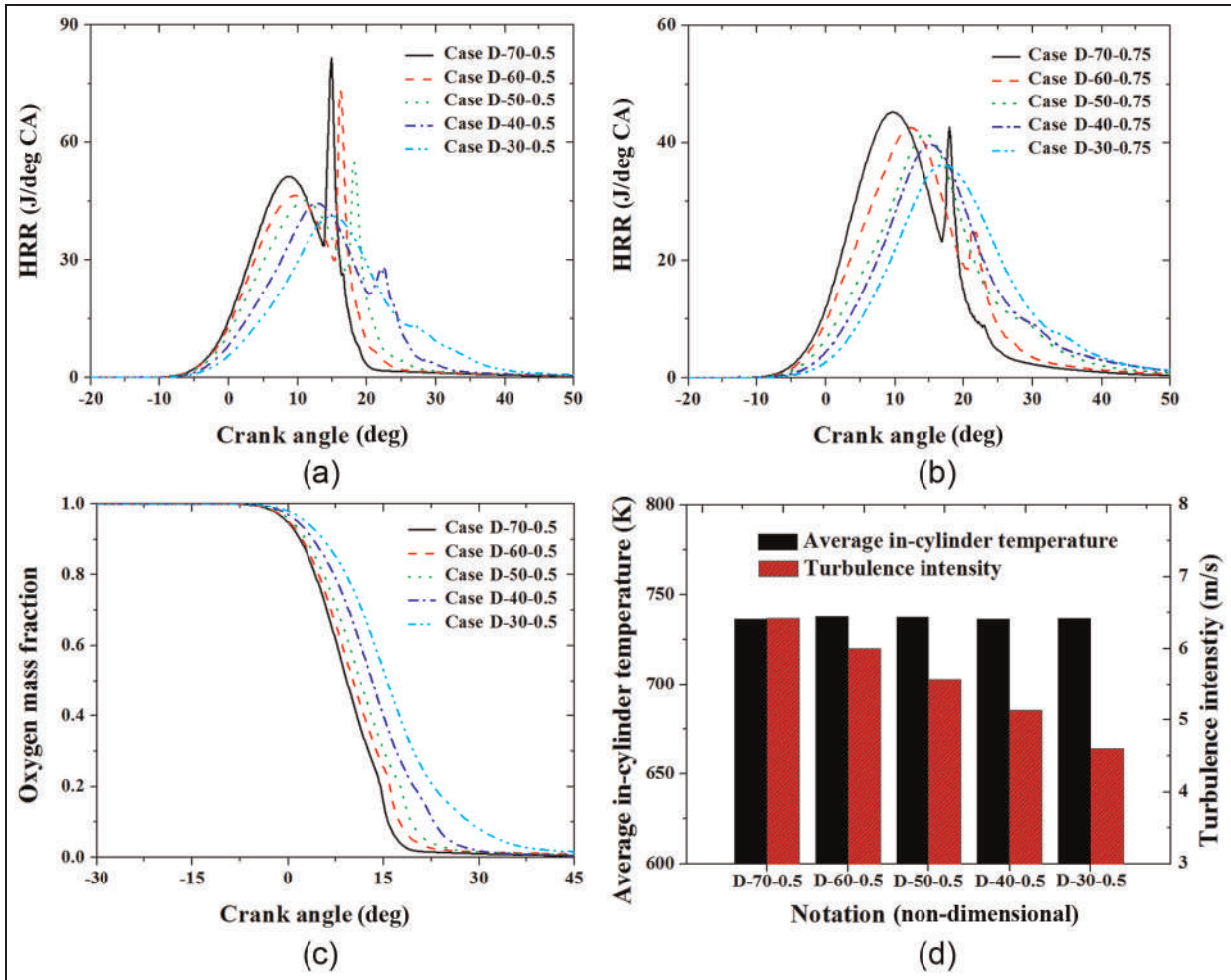


Figure 10. (a), (b) Knock detection by the HRR at injection duration ratios of (a) 0.5 and (b) 0.75. (c) The oxygen mass fraction at an injection duration ratio of 0.5 to represent the combustion speed. (d) The in-cylinder temperature and the turbulence intensity at an injection duration ratio of 0.5.
HRR: heat release rate; CA: crank angle.

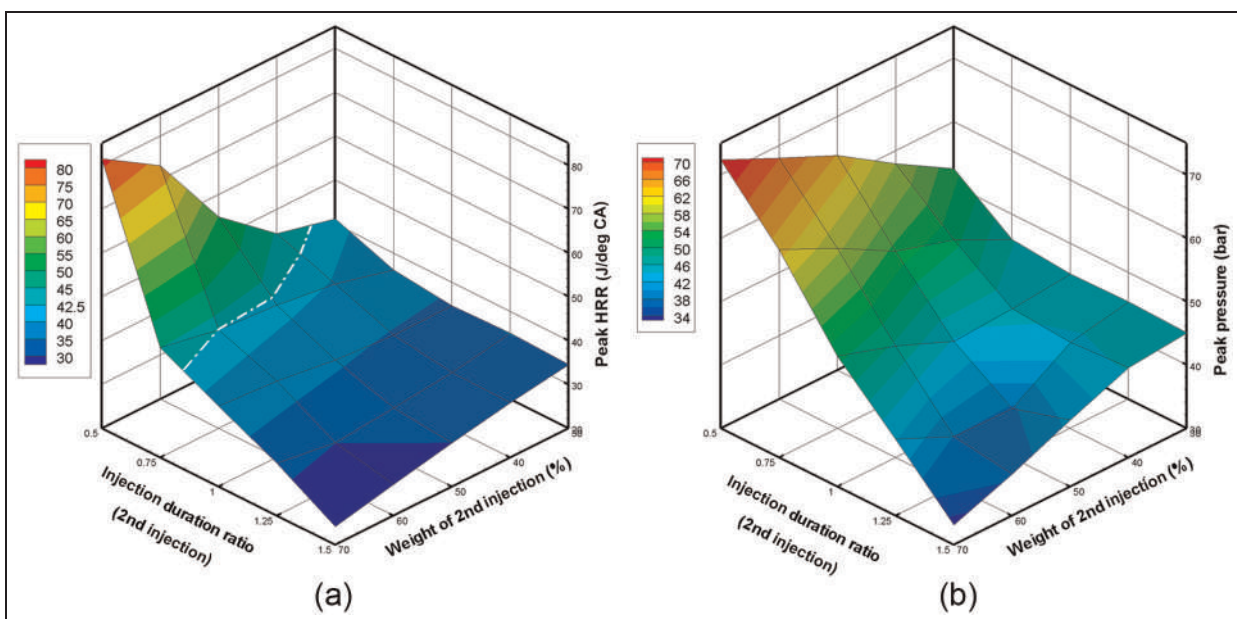


Figure 11. Contour plots of (a) the peak HRR and (b) the peak in-cylinder pressure as functions of the injection duration ratio and the weight of the second injection.
HRR: heat release rate; CA: crank angle.

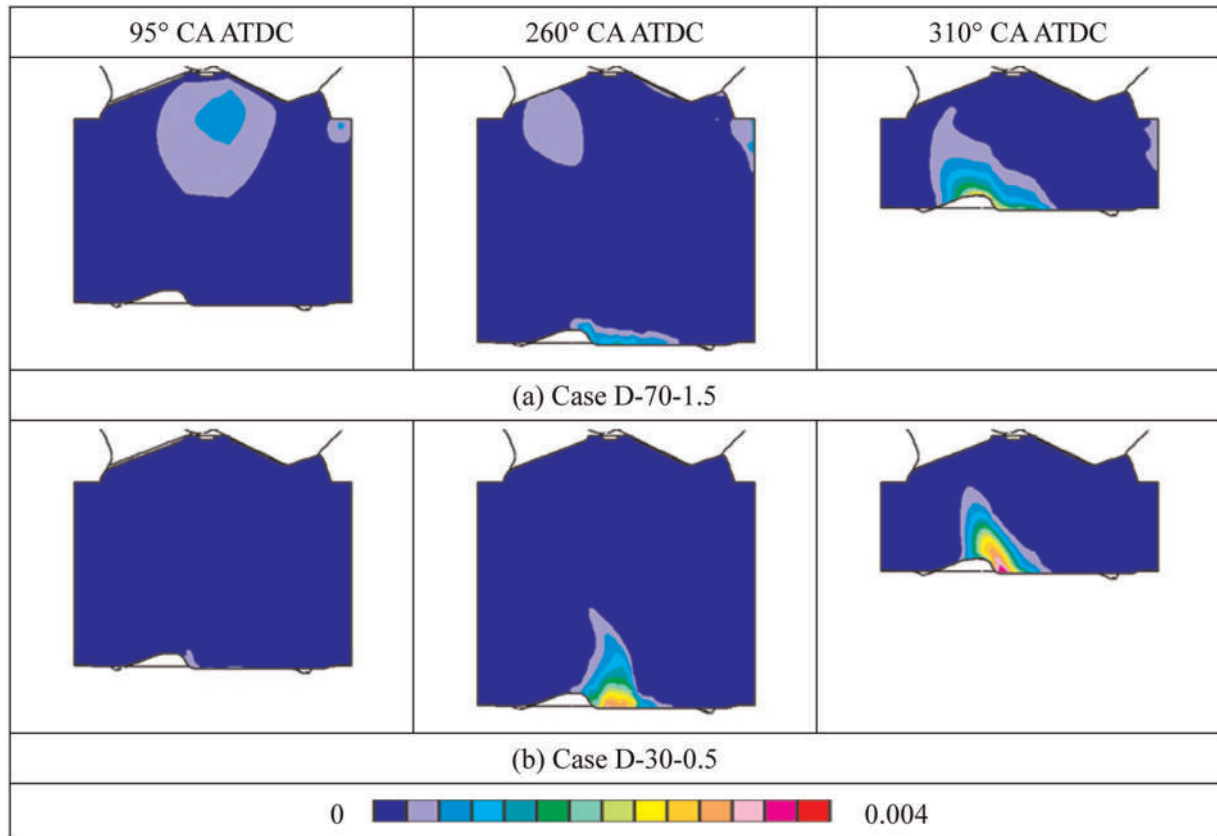


Figure 12. Progress of soot generation distinguished by two scenarios, showing the distributions of the soot mass fractions: (a) caused by a locally rich gaseous mixture and a pool fire (case D-70-1.5); (b) cause by only a pool fire (case D-30-0.5). CA: crank angle; ATDC: after top dead centre.

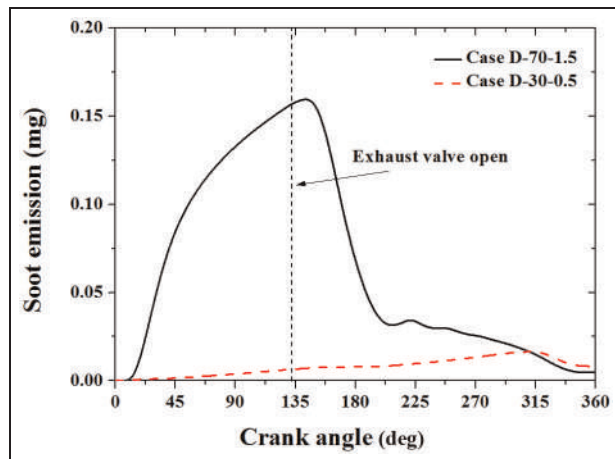


Figure 13. Soot mass histories for case D-70-1.5 and case D-70-0.5 during combustion and the exhaust stroke.

shown with different weights of the second injection had similar tendencies. When the first scenario occurred, soot generation by the locally rich gaseous mixture was dominant, approaching a maximum value during the combustion stroke immediately after the exhaust valve activated. On the other hand, for case D-30-0.5 when the second scenario occurred, soot

generation by the pool fire dominated during the exhaust stroke. The locally rich gaseous mixture generated much more soot than did the pool fire.

Figure 14(a) to (i) shows the configurations on the y axis and the z axis of the soot mass fractions within the combustion chamber. The observation point was 110° CA after top dead centre (ATDC) before the exhaust valve activated, where the locally rich gaseous mixture was dominant. The z -axis plane is a top view of the combustion chamber. The soot inside the combustion chamber had images corresponding to those for the excess air ratio distribution (shown in Figure 6), indicating that, the larger the values of the injection weight and the injection duration ratio, the greater the amount of soot generated. Moreover, the result indicates that the combustion process was incomplete owing to generation of much more soot; the results of a relatively low pressure also provide further evidence of this. The greatest amount of soot was generated for case D-70-1.5, but almost no generation of soot due to a locally rich gaseous mixture was detected in the cases with an injection duration ratio of 0.5. Figure 15 shows the configurations on the y axis and the z axis of the soot mass fractions within the combustion chamber at 280° CA ATDC, where soot generation by a pool fire was dominant. In this case, the z -axis plane was on the

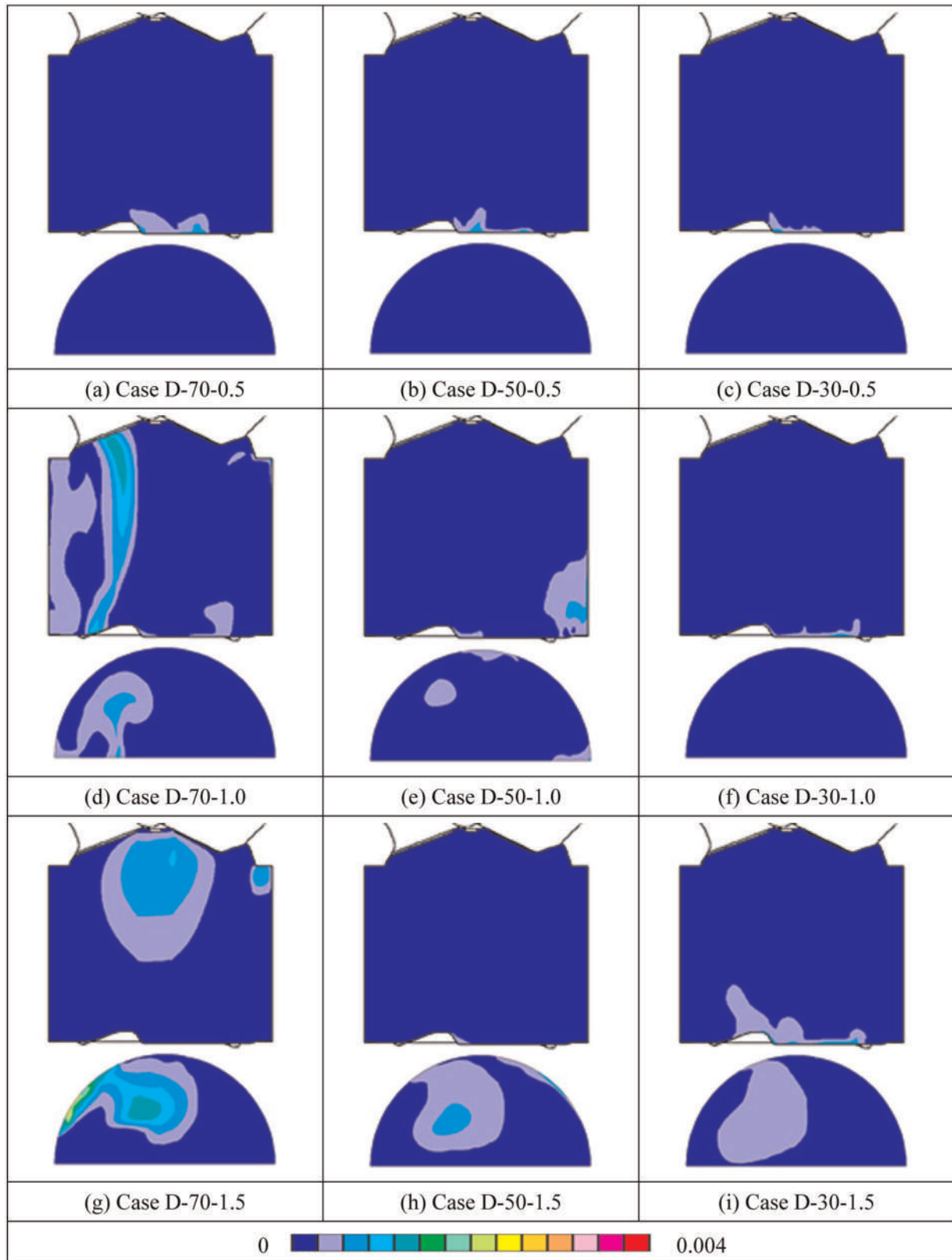


Figure 14. Images of the soot mass fraction within the combustion chamber on the y axis and the z axis before exhaust valve activation for various cases (110° CA ATDC).

piston surface, differing from Figure 14, in which the plane was situated in the middle of the chamber. The areas inside the red dashed lines represent the deposited

soot generated by incomplete combustion; the effects of these areas are excluded in order to examine the sole effect of the fuel film burning. For each injection

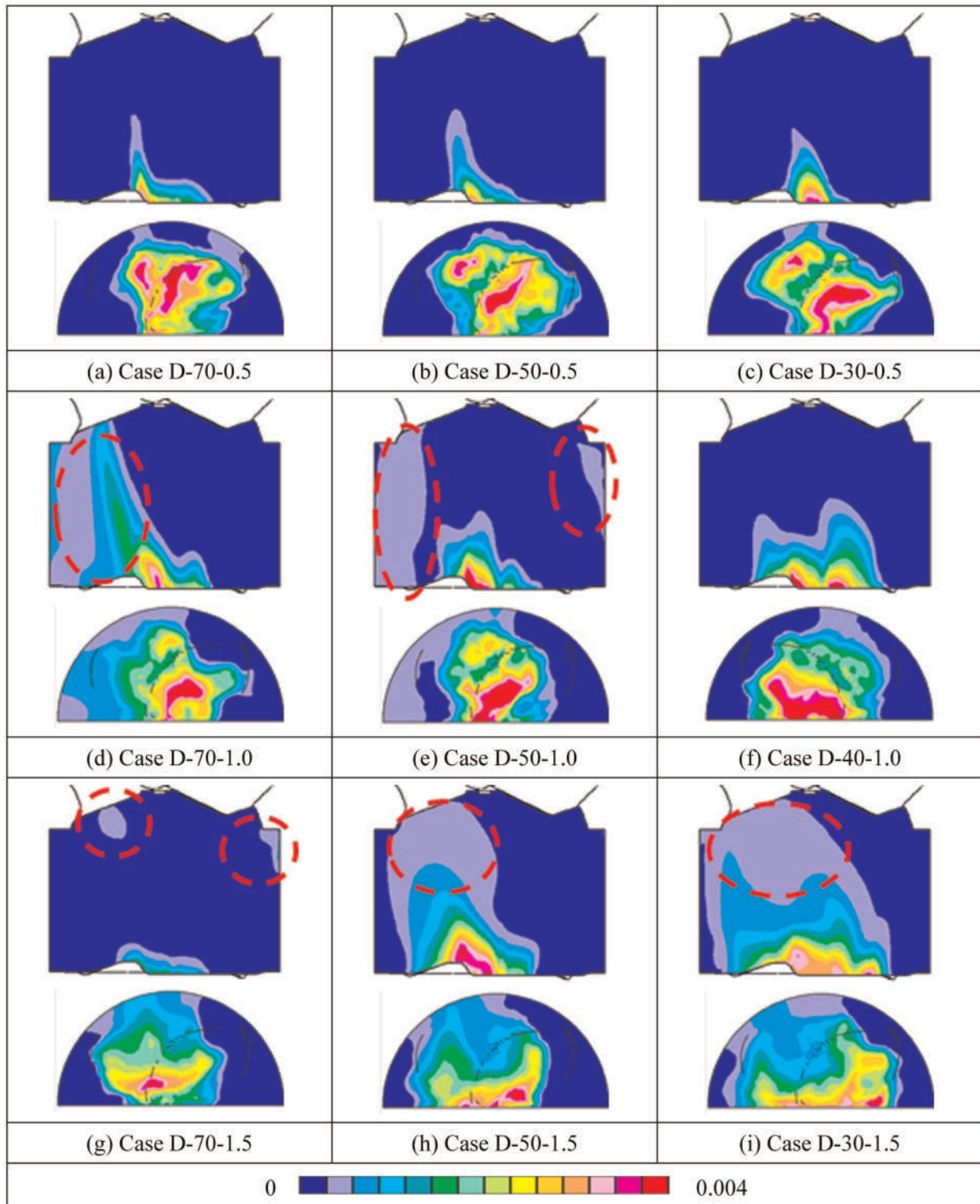


Figure 15. Images of the soot mass fraction within the combustion chamber on the y axis and on the piston surface for various cases (280° CA ATDC).

duration ratio, the soot formation increased as the weight of the second injection was decreased by the influence of the LFF. However, the effect of the injection duration ratio was difficult to identify because the LFF was less affected by this parameter.

Figure 16(a) and (b) shows the peak value of the generated soot and the carbon dioxide (CO_2) engine-out

emissions respectively within the combustion chamber at 132° CA ATDC during the exhaust stroke. The soot and CO_2 engine-out emissions appear to have opposite overall tendencies. When the weight of the second injection or the injection duration ratio increased, the overall soot emissions dramatically increased, but the CO_2 emissions decreased. The soot emissions were less

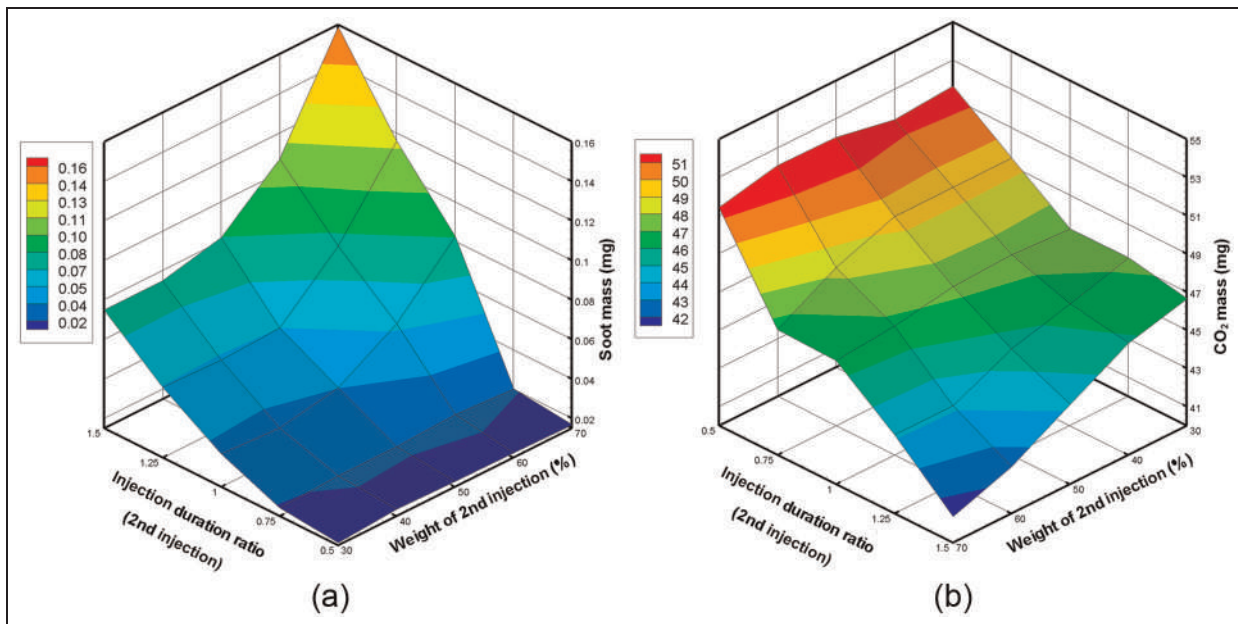


Figure 16. Contour plots of (a) the soot engine-out emissions and (b) the CO₂ engine-out emissions as functions of the injection duration ratio and the weight of the second injection.

influenced by the weight of the second injection in the region of low injection duration ratios (0.5 and 0.75) but maximally grew approximately tenfold with the smallest case (case D-70-0.5). The poor mixture induced poor combustion, which influenced the pressure, the HRR and the soot and CO₂ emissions. Therefore, the LFF affects the formation of soot emissions, but the dominant effect was the excess air ratio mixture.

Conclusions

This paper deals with analysis of the impingement of fuel sprays and the fuel–air mixing distribution in a four-stroke spark ignition gasoline DISI engine. The results showed how fuel impingement and mixing formation affect the combustion characteristics with variations in the injection duration ratio of the second pulse injection and the weight of the second pulse injection. The conclusions can be summarized as follows.

1. The amount of LFF was influenced by the weight of the second pulse injection, appearing to have 31.7–37.5% less formation on the piston surface as the weight of the second pulse injection increased. However, the amount of LFF had a varying range from approximately 1% to 4% and was influenced by the injection duration ratio. The injection duration ratio of the second pulse injection had appropriate conditions near the injection duration ratio of 1.0, which minimized the LFF.
2. The LFF on the piston surface induces soot formation owing to the pool fire, which appears to generate a greater amount of soot when a sufficient amount of LFF film impinged on the piston surface.

3. However, the fuel–air mixture was the most prominent factor in determining the overall combustion characteristics. The appropriated excess air ratio distribution (excess air ratio values near 1.0) near the spark plug induces a higher pressure and a higher HRR. Also, the cases with a poor fuel–air mixture had more overall soot formation, even though soot formation from the LFF was less than in the other cases (e.g. case D-70-1.5).
4. A split injection without optimization can cause poor combustion characteristics such as knocking, incomplete combustion and soot engine-out emissions but can also increase the thermal efficiency and the fuel economy. The most appropriate case was case D-30-0.5.

Declaration of conflicting interest

The authors declare that there is no conflict of interest.

Funding

This research was supported by the Strategy Industrial Technology Development Project of Korea Evaluation Institute of Industrial Technology (10035392-2012-03).

References

1. Xu M and Markle LE. CFD-aided development of spray for an outwardly opening direct injection gasoline injector. SAE paper 980493, 1998.
2. Nauwerck A, Pfeil J, Velji A et al. A basic experimental study of gasoline direct injection at significantly high injection pressures. SAE paper 2005-01-0098, 2005.
3. Anderson W, Yang J, Brehob DD et al. Understanding the thermodynamics of direct-injection spark-ignition

- (DISI) combustion systems: an analytical and experimental investigation. SAE paper 962018, 1996.
4. Han Z, Reitz RD, Yang J, et al. Effects of injection timing on air–fuel mixing in a direct-injection spark-ignition engine. SAE paper 970625, 1997.
 5. Grimaldi F, Gervais D, Marchal A et al. Single-cylinder experiments for downsizing-oriented SI concept: GDI and VVL thermodynamic comparison. SAE paper 2007-24-0013, 2007.
 6. Westrate B, Warren C, Vanderwege B et al. Dynamometer development results for a stratified-charge DISI combustion system. SAE paper 2002-01-2657, 2002.
 7. Zhao F, Lai MC and Harrington DL. Automotive spark-ignited direct-injection gasoline engines. *Prog Energy Combust Sci* 1999; 25(5): 437–562.
 8. Desoutter G, Cuenot B, Habchi C et al. Interaction of a premixed flame with a liquid fuel film on a wall. *Proc Combust Inst* 2005; 30(1): 259–266.
 9. Stanglmaier RH, Li J and Matthews RD. The effect of in-cylinder wall wetting location on the HC emissions from SI engines. SAE paper 1999-01-0502, 1999.
 10. Stojkovic BD, Fansler TD, Drake MC et al. High-speed imaging of OH* and soot temperature and concentration in a stratified-charge direct-injection gasoline engine. *Proc Combust Inst* 2005; 30(2): 2657–2665.
 11. Stevens E and Steeper R. Piston wetting in an optical DISI engine: fuel films, pool fires, and soot generation. SAE paper 2001-01-1203, 2001.
 12. Han Z, Yi J and Trigui N. Stratified mixture formation and piston surface wetting in a DISI engine. SAE paper 2002-01-2655, 2002.
 13. Drake MC, Fansler TD, Solomon AS et al. Piston fuel films as a source of smoke and hydrocarbon emissions from a wall-controlled spark-ignited direct-injection engine. SAE paper 2003-01-0547, 2003.
 14. Park S and Ghandhi JB. Fuel film temperature and thickness measurements on the piston crown of a direct-injection spark-ignition engine. SAE paper 2005-01-0649, 2005.
 15. Behnia M and Milton BE. Fundamentals of fuel film formation and motion in SI engine induction systems. *Energy Conversion Managmt* 2001(15–17); 42: 1751–1768.
 16. Nemecek LM, Wagner RM and Drallmeier JA. Fuel droplet entrainment studies for minimization of cold-start wall-wetting. SAE paper 950508, 1995.
 17. Shayler PJ, Colechin MJF and Scarisbrick A. Fuel film evaporation and heat transfer in the intake port of an SI engine. SAE paper 961120, 1996.
 18. Ma H, Marshall S, Stevens R et al. Full-bore crank-angle resolved imaging of combustion in a four-stroke gasoline direct injection engine. *Proc IMechE Part D: J Automobile Engineering* 2007; 221(10): 1305–1320.
 19. Fan Q, Li L, Hu Z et al. Spray characteristics and wall-impingement process with different piston tops for the multi-hole injector of DISI gasoline engines. SAE paper 2011-01-1222, 2011.
 20. Serras-Pereira J, Aleiferis PG and Richardson D. Imaging and heat flux measurements of wall impinging sprays of hydrocarbons and alcohols in a direct-injection spark-ignition engine. *Fuel* 2012; 91(1): 264–297.
 21. Yi J, Han Z, Xu Z et al. Combustion improvement of a light stratified-charge direct injection engine. SAE paper 2004-01-0546, 2004.
 22. Yang J and Anderson RW. Fuel injection strategies to increase full-load torque output of a direct-injection SI engine. SAE paper 980495, 1998.
 23. Stiesch G, Merker GP, Tan Z et al. Modeling the effect of split injections on DISI engine performance. SAE paper 2001-01-0965, 2001.
 24. Li T, Nishida K, Zhang Y et al. Enhancement of stratified charge for DISI engines through split injection. *JSME Int J Ser B* 2005; 48(4): 687–694.
 25. Park C, Kim S, Kim H et al. Effect of a split-injection strategy on the performance of stratified lean combustion for a gasoline direct-injection engine. *Proc IMechE Part D: J Automobile Engineering* 2011; 225(10): 1415–1426.
 26. Costa M, Sorge U and Allocca L. Increasing energy efficiency of a gasoline direct injection engine through optimal synchronization of single or double injection strategies. *Energy Conversion Managmt* 2012; 60: 77–86.
 27. Leduc P, Dubar B, Ranini A et al. Downsizing of gasoline engine: an efficient way to reduce CO₂ emissions. *Oil Gas Sci Technol* 2003; 58(1): 115–127.
 28. Lake T, Stokes J, Murphy R, et al. Turbocharging concepts for downsized DI gasoline engines. SAE paper 2004-01-0036, 2004.
 29. Clenci A, Descombes G, Podevin P et al. Some aspects concerning the combination of downsizing with turbocharging, variable compression ratio, and variable intake valve lift. *Proc IMechE Part D: J Automobile Engineering* 2007; 221(10): 1287–1294.
 30. Yuen MC and Chen LW. On drag of evaporating liquid droplets. *Combust Sci Technol* 1976; 14(4–6): 147–154.
 31. Reitz RD and Diwakar R. Effect of drop breakup on fuel sprays. SAE paper 860469, 1986.
 32. Bai C and Gosman AD. Development of methodology for spray impingement simulation. SAE paper 950283, 1995.
 33. Bai C. *Modelling of spray impingement processes*. PhD Thesis, University of London, London, UK, 1996.
 34. O'Rourke PJ. *Collective drop effects on vaporizing liquid sprays*. PhD Thesis, University of Princeton, Princeton, New Jersey, USA, 1981.
 35. Yakhot V, Orszag SA, Thangam S et al. Development of turbulence models for shear flows by a double expansion technique. *Phys Fluids A* 1992; 4: 1510–1520.
 36. Colin O, Benkenida A and Angelberger C. 3D modeling of mixing, ignition and combustion phenomena in highly stratified gasoline engines. *Oil Gas Sci Technol* 2003; 58(1): 47–62.
 37. Colin O and Benkenida A. The 3-zones extended coherent flame model (ECFM3Z) for computing premixed/diffusion combustion. *Oil Gas Sci Technol* 2004; 59(4): 593–609.
 38. Metghalchi M and Keck JC. Burning velocities of mixtures of air with methanol, isoctane, and indolene at high pressure and temperature. *Combust Flame* 1982; 48: 191–210.
 39. Patterson MA, Kong S-C, Hampson GJ et al. Modeling the effects of fuel injection characteristics on diesel engine soot and NO_x emissions. SAE paper 940523, 1994.
 40. Han SB, Lee NH and Lee S. A study on the unsteady temperature field of combustion chamber wall in a turbocharged gasoline engine. *J Mech Sci Technol* 1996; 10(4): 518–525.
 41. Prasad R and Samria N. Heat transfer and stress fields in the inlet and exhaust valves of a semi-adiabatic diesel engine. *Comput Struct* 1990; 34(5): 765–777.

42. Serras-Pereira J, van Romunde ZR, Aleiferis PG et al. Cavitation, primary break-up and flash boiling of gasoline, iso-octane and *n*-pentane with a real-size optical direct-injection nozzle. *Fuel* 2010; 89(9): 2592–2607.
43. Aleiferis PG and van Romunde ZR. An analysis of spray development with iso-octane, *n*-pentane, gasoline, ethanol and *n*-butanol from a multi-hole injector under hot fuel conditions. *Fuel* 2013; 105: 143–168.
44. Asproulis P. *High resolution numerical predictions of hypersonic flows on unstructured meshes*. PhD Thesis, University of London, London, UK, 1994.
45. Mattarelli E, Borghi M, Balestrazzi D et al. The influence of swirl control strategies on the intake flow in four valve HSDI diesel engines. SAE paper 2004-01-0112, 2004.
46. Weltens H, Bressler H, Terres F et al. Optimisation of catalytic converter gas flow distribution by CFD prediction. SAE paper 930780, 1993.